RSC Advances

ROYAL SOCIETY OF CHEMISTRY

www.rsc.org/advances

Dendrimer templated bioactive glass ceramic nanovehicle for gene delivery applications

Nidhi Gupta[1], Deenan Santhiya[1*], Anusha Aditya[2] and Kishore Badra[1]

[1]Delhi Technological University, Department of Applied Chemistry and Polymer Technology, Bawana Road, Delhi-110 042, India

[2]Institute of Genomics and Integrative Biology (CSIR), Mathura Road, Delhi-110025, India

∗Corresponding author Tel: +91 9958580295

E-mail addresses: deenan.santhiya@dce.ac.in

Abstract

In the present investigation, multifunctional nanocrystalline microporous 45S5 bioglass particles were synthesized using poly (amidoamine) (PAMAM) dendrimer generation 3 as a template. Apart from bone regeneration ability, special focus has been placed on its application as a nanocarrier in gene delivery. For considering, bio-inspired nanoscale microporous 45S5 bioglass (BG) as a bone regenerative material, evaluating biocompatibility and mechanical properties are the essential parameters. Initially, characterization of BG was carried out for its morphology, composition and textural study. Interestingly, polygonal shape was observed by TEM and microporosity was further confirmed by BET analysis. The mechanical properties of obtained glass-ceramics was evaluated by dynamic mechanical analyzer (DMA) which reveals its stiffness and good damping property. The nanocrystalline BG was observed to be osteoproductive through the hydroxycarbonated apatite (HCA) formation in simulated body fluid (SBF). Biocompatibility of the material was confirmed by the MTT assay and further the U2OS osteosarcoma cells proliferation on the surface of the BG was visualized by FESEM. The material was found to be highly cell proliferative. In addition to this, *in-vitro* studies were carried out to evaluate the therapeutic pDNA compaction ability of the bioglass material. Further, the transfection ability of the material was also investigated against the CHO-K1 cell line. This investigation provides a new insight into the application of bioactive glass as an efficient non-viral nanocarrier for gene therapy.

Keywords: nanocarrier, gene delivey, bioactive glass, bone regeneration

1. Introduction

Poor lifestyle, health history and population ageing are the primary causes responsible for the gradual degeneration of bone; making strongest part of the body so fragile that even a small accident can result in its fracture. Literature reveals existence of a considerable variety of bone implant materials for bone therapy. Porous bioactive glass, a third generation biomaterials are the one among them which are extensively known for bone regeneration.[1-3] However, low fracture toughness and mechanical strength, especially in porous form of these materials limits its load bearing applications. Thus considering knowledge of mechanical properties of bioglass is of major importance for the design of fracture fixation devices, as well as the design, fixation, and survival of artificial joints.[4]

Currently there has been considerable interest in the nanoscale biomaterials in view of their biomimetic nano-dimensions and properties comparable to natural tissues such as bone.[5] Various researchers have reported nanoscale bioactive glass materials of different morphologies. Nanospheres,[6-8] nanofibers,[9] nanopowders[10] are a few such examples. These high-surface biomaterials exhibits an enhanced biocompatibility, bioactivity,[6] mechanical stability[11] and increases the dissolution rate[12] which accelerates the deposition process of hydroxyapatite[13] as the particle size decreases. Decrease in dimension promotes cell interaction,[14,15] biomineralization process, protein adhesion, enhances osteoblast proliferation, and engenders the anti-microbial and anti-inflammatory properties.[7,8,16] It also makes it easily injectable at bone defect sites in comparison to micron-sized. Advanced applications of these hierarchical bioactive nanoglass particles in the field of cell tracking and intracellular delivery of therapeutic molecules such as drugs, growth factors, nucleic acids and small interfering RNA have been currently focused[7,8,17-20] highlighting the importance of multifunctional ability of the bioglass. Apart from bone regrowth along with angiogenesis, recently bioglass also finds application in soft tissue engineering including wound dressing, lung tissue repair, gastrointestinal and nerve regeneration.[3] Recently its application in the destruction of bone tumors have also been reflected.[20,21]

A limited literature exists on gene transfection ability of BG nanoparticles in the field of non-viral gene therapy, a promising approach for delivering therapeutic genes to specific bone

tissues for regeneration. Among the existing transfection system, non-viral vectors such as cationic polymers or liposomes are considered very effective as *in vitro* transfection agents but often display poor *in vivo* transfection efficiency due to their aggregation in serum and to non-specific and extracellular adhesion molecules.[22] Even the surface functionalization is limited, which resist in targeted delivery. In order to overcome these shortcomings, inorganic nanoparticles such as silica could be a better option. But their unresolved toxicity and aggregation issues limits their applicability as a suitable vector. Apart from this, their disadvantage, being the necessity of considering the degradability of the inorganic nanoparticles in the system. However, no such parameter is an issue for the bioactive glass nanoparticles. Since the different dissolution products of the bioglass material are associated with the gene stimulation either upregulated or downregulated for the bone regeneration. Various ion contents of the bioglass such as phosphate ions are responsible for the calcium phosphate deposition, Si is important for the osteoblast formation while sodium content of the bioglass ease the dissolution rate of the bioglass nanoparticle.[14]

Recently, capability of BG nanoparticles as gene transfection agents have been tested by few researchers such as radial mesoporous bioactive glass has been reported to be efficient carriers to deliver osteoactivin gene.[23] BG nanoparticles have also been reported as siRNA carriers with a transfection efficiency as high as 80%.[18] Still the study in respect of gene delivery capability of the bioglass nanoparticle is at nascent stage. Further, experiments need to be conducted to establish the correlation between the textural property and gene delivery capability of the bioglass nanoparticle. More interestingly, these resorbable bioactive glass constructs are also being recently researched to influence gene expressions at the local environment by manipulating material properties such as surface chemistry, topography and the release of dissolution ions.[24] In this respect, in the following paper as per our knowledge a first attempt is carried out to study the gene delivery capability of the microporous bioglass nanoparticles in comparison with the mesoporous bioglass nanoparticles.

Required superior textural properties of these bioactive glass materials to function as an effective nanocarrier could be better achieved through bio-inspired route.[25] Self-organization and directed assembly of biological macromolecules plays an important role in the creation of the nanostructured materials, generally found in biology. In biology, there exists abundant of

structures with nanoscale dimensions, and virtually all the functions provided by these materials are a direct consequence of the nanoscale dimension of the structure. Few examples include proteins, DNA, actin, spider silk and so on.[26] Because of the limited variety of materials available by purely biological routes, there is great interest in utilizing the sophistication offered by biological system in concert with synthetic procedures to create materials with otherwise unobtainable nanostructures and thus, potentially, unique properties. Using this route different ceramic oxides such as ZnO have been synthesized using different biomolecules such as DNA[27] and gelatin[28] as a template. Taking inspiration from nature, in the present work, we propose to synthesize bioactive material through bioinspired route by mimicking physiological conditions in the laboratory as reported by Santhiya *et al*.[29]

In this regard, polyamidoamine (PAMAM) dendrimers, mimics of micelles and proteins, have attracted increasing interest for the regulation of inorganic compounds due to their synthetically tunable molecular structure, size, surface charge as well as functionality.[30,31] Such compounds have been used to mineralize many inorganic compounds such as $BaWO_4$ of right square prism as well as spherical crystals depending on generation number[32] at low temperature. Hence, it is postulated that dendrimer is an interesting template to synthesize hierarchical nanostructured bioactive glasses.

Considering these interesting advanced applications, in this investigation we report the synthesis of multifunctional nanoscale microporous bioactive glass ceramic using poly (amidoamine) dendrimer generation 3 (PAMAM G3) as a structure directing agent at ambient condition. The obtained material was subjected to intensive characterization analysis. The mechanical features of the nanomaterial were evaluated by dynamic mechanical analyzer (DMA). The *in vitro* cytocompatability of the bioglass sample was examined using U2OS osteoblast-like osteosarcoma cells by 3-(4,5-dimethylthiazol-2-yl)-2,5-diphenyltetrazolium bromide (MTT) assay. Spreading pattern of osteosarcoma cells over the as prepared bioglass surface was also evaluated. Additionally, advanced function of the bioglass material as a nanocarrier for therapeutic gene was also monitored by interacting bioglass nanoparticles with plasmid DNA (pDNA) and transfecting the same, with the CHO-K1 cell lines.

2. Materials and Methods

2.1. Materials

The precursors used for the development of bioactive glass ceramics, namely tetraethyl orthosilicate (TEOS), triethyl phosphate (TEP), sodium acetate, calcium acetate and surface directing agent PAMAM dendrimer were purchased from Sigma-Aldrich with purity of 99%. They were used directly without further purification. U2OS, a human osteoblast-like osteosarcoma cell line (ATCC) was obtained from NIA, Delhi. DMEM medium was procured from Sigma-Aldrich for the cell growth. The chemicals required for the cytocompatability assay such as 3-(4,5-dimethylthiazol-2-yl)-2,5-diphenyltetrazoliumbromide (MTT), sodium dodecyl sulphonate and isopropanol were also purchased from Sigma-Aldrich. Therapeutic pEGFP-C1 plasmid DNA was used for the *in-vitro* nucleic acid interaction studies with the bioactive glass particles. The plasmid pEGFP-C1 4.7kb (Clontech) were amplified in Escherichia coli Mach1 T1 while pMIR-REPORT™Luciferase, 6.47 kb (Ambion) were amplified in E.coli DH5-α and both were purified using GenElute HP Endotoxin-Free Plasmid MaxiPrep kit (Sigma). Luciferase assay kit was purchased from Promega. For all the experimental work, milli-Q water was used and all other reagents used were of analytical reagent (AR) grade. All other chemicals and cell culture media were procured from Sigma, unless mentioned otherwise.

2.2 Methods

Bioactive glass Synthesis: The bioactive glass ceramic was synthesized by bio-inspired route as reported by Santhiya *et al*.[29] In brief, sequentially the precursors, namely 9.29 g of tetraethyl orthosilicate, 1.0 g of triethyl phosphate, 6.36 g of sodium acetate, and 4.21 g of calcium acetate, were added gradually at an interval of 30 min into 100 ml of 10 mM TRIZMA buffer solution containing required amount of surface directing agent PAMAM dendrimer generation 3 at pH 8 with constant stirring at 37 °C in a silicone oil bath for 24 h. After 24 h, a white precipitate was obtained, centrifuged, washed with milli-Q water and dried at 40 °C in an air oven for 48 h and preserved in desiccator for further use. Textural tunability of the bioglass material has been achieved by using different concentration of PAMAM dendrimer. Namely, concentrations of 5, 15 and 35 mM of PAMAM dendrimer were studied. Of which at 15 mM we could achieve particles of our interest. So, further studies were carried out at 15mM of PAMAM dendrimer (For details, refer ESI. S2). Before subjecting to various characterization methods, the bioglass

sample was lyophilized to remove the moisture content of the sample, if any. The bioglass sample before and after lyophilization was subjected to thermogravimetric analysis (TGA) using Perkin Elmer, Pyris Diamond TGA/DTA.

XRD Measurement: To evaluate the crystalline and amorphous nature of the sample powder X-ray diffraction experiments were performed with Bruker D4 X-ray diffractometer operating at 30 kV and 15 mA using CuKα radiation. XRD patterns were collected in the 2θ range of 10° to 70° with step sizes of 0.02° and a counting time of 6 s per step.

FTIR Recording: Fourier transform infrared (FTIR) spectra were recorded for the bioactive glass samples. Dried samples were ground and mixed thoroughly with potassium bromide at the ratio of 1:100 and pelleted. The IR spectra of the pellets were then recorded using the NICOLET 380 FTIR operating in the range of 400–4000 cm^{-1} with the resolution of 4 cm^{-1}. For the mechanistic study of bioglass formation as per the synthetic procedure mentioned above, FTIR spectra of the reaction mixture for each of the sequentially added precursor interaction on dendrimer template were studied using Perkin Elmer Model Spectrum RXI-Mid IR.

Morphology Study: The surface morphology of bioactive glass-ceramics was characterized by thermal field emission gun scanning electron microscopy (FEI Quanta 200F). The samples were gold coated and then observed at an accelerating voltage of 12 KeV. The elemental analysis of bioglass sample (BIS-nBG-DG3) was carried out by energy dispersive X-ray spectroscopy (Oxford X-MAX) and results were collected at 20 keV. Additionally, the morphology and SAED pattern was characterized using JEOL transmission electron microscope (JEM-2100F) field emission type at an accelerating voltage of 200 KV.

Porosity Study: Porosity of the lyophilized sample was evaluated using TEM and BET. TEM was recorded for the lyophilized bioglass sample after staining with 1% uranyl acetate and was then examined under TEM (Tecnai G2 twin (FEI)) operating at an acceleration voltage of 80 kV. The textural properties of the Bioglass ceramic was also then determined by nitrogen adsorption–desorption analyses at -196°C using a Quantachrome Autosorb-1C TCD analyzer (Model ASIC-

X-TCD6) and with nitrogen as adsorptive gas (N_2, cross sectional area 0.162 nm^2). As per the standard BET protocol, before analysis, the sample was degassed under vacuum at 200 °C for 6 h. The surface area was determined using the Brunauer–Emmett–Teller (BET) equation on the nitrogen adsorption data obtained. The pore-size distribution was determined by the Barret–Joyner–Halenda (BJH) method applied to the desorption branch of the isotherm. In order to bring out the differences in the porosity nature of the bioglass after degassing of the lyophilized sample, the as prepared bioglass sample (before lyophilization) was subjected to heating at 200 °C for 3 h and then subjected to TGA, BET and TEM analyzes.

Density Test: Density measurements of BIS-nBG-DG3 sample were determined by using ethanol as the displacement medium in a DENVER Instrument SI-234 analytical balance.

Zeta Potential Measurement: Zeta-potential value of the as synthesized BIS-nBG-DG3 material was measured in trizma buffer pH8 using ZetasizerNano ZS (Malvern Instruments, UK) instrument. A minimum of 3 readings were recorded for the sample.

Bioactivity Test: An *in vitro* evaluation of the bone forming activity of the sample was performed in simulated body fluid (SBF) by monitoring the formation of bone-like hydroxyapatite on the surface of the bioglass. To check the bioactivity of the sample, it was incubated in SBF medium as per the procedure described by Kokubo *et al* [33] for different intervals of periods (ESI S1.1).

Cell studies: Biocompatibility of the human osteoblast like sarcoma cells was evaluated using two methods: the elution test method (ISO 10993-5), and by growing the cells on the pellet. Cell studies were carried out using U2OS, a human osteoblast-like osteosarcoma cell line (ATCC). The detailed procedure can be found in ESI S1.2.

Mechanical Test: All viscoelastic measurements were performed using Perkin Elmer DMA 8000, equipped with material pocket. Dynamic mechanical analyzer (DMA) is a non-destructive and an adequate technique for characterizing the mechanical features of the biomaterials.[34] The measurements were carried out at 37 ^oC. The powder sample was filled into a material pocket of DMA with 0.27 mm thickness and 6 mm width (measured each sample accurately with a micrometer). The experiments were performed by measuring the sample in the DMA before and after immersion in SBF for 30 days. The geometry of the sample within material pocket was then measured by a micrometer and pocket was clamped in the DMA apparatus (the distance between

the clamps was 10 mm) in a single point bending mode. After equilibration at 37^{o}C, the DMA spectra were obtained during a frequency scan between 0.1 and 10 Hz. The experiments were performed under constant strain amplitude (0.03 mm) and a strain of 5%. Three specimens were tested for each condition.

In-vitro studies on bioglass nanoparticle-pDNA interaction: Initially, the dried bioglass nanoparticle sample was aminated using 3-amino-propyl triethoxysilane (APTES) as per the procedure described else-where.[18] The so obtained aminated bioglass material was also subjected to various characterization techniques such as FTIR, Zeta Potential, TEM and CHNSO (Elementar Analysensysteme Germany, Vario Micro Cube). The biophysical studies were carried out for pDNA:aminated bioglass nanoparticle interaction at the weight ratio of 1:0, 1:10, 1:20, 1:30, 1:40, 1:50, 1:60, 1:70, 1:80, 1:90, 1:100 (µg:µg) respectively as per the standard procedure followed in literature.[35,36] The electrophoretic mobilities of the pDNA:ABG complex prepared at various weight ratio were determined using 1% agarose gel electrophoresis. Circular dichroism (CD) spectra of pDNA in the absence and presence of aminated bioglass nanoparticle were recorded between 200 and 325 nm in a Jasco spectropolarimeter (model 715) equipped with a peltier thermostat. The UV melting profiles of the pDNA:ABG nanocomplex were monitored using Cary 100 concentration UV-visible spectrophotometer. The pDNA:ABG nanocomplex was visualized under atomic force microscope (AFM), Agilent Technologies. The images were obtained in tapping mode in air with 225-µm-long silicon cantilevers.

Transfection studies: The *in vitro* study of the complexation ability of reported bioglass material with the pDNA has been extended to the transfection ability of the same against the CHO-K1 cell line, using lipofectamine as a control sample. Transfection efficiency of pDNA:ABG complex at the weight ratio of 1:50, 1:100, 1:125, 1:150 and 1:175 has been demonstrated by luciferase assay. For the luciferase assay, the pDNA used was pMIR-REPORT™ Luciferase DNA capable of expressing bioluminescent luciferase enzyme. Bioluminescent reporter is potent to characterize the enormous complexity of living systems. Even capable to deliver 10- to 1,000-fold higher assay sensitivity than fluorescent reporters such as GFP (Green Fluorescent Protein)[37]. The detailed procedure can be found in ESI S1.3. The cell morphology was also observed after 24 h interaction with the pDNA/ABG complex under the Floid Cell Imaging Station microscope (Life Technologies).

3. Results and Discussion

3.1. Morphological, Structural and Textural Characterization

The synthesized bioglass sample was subjected to wide angle X-ray diffraction analysis and result is displayed in Fig. 1. The broad peak at 2θ degree values ranging from 15° to 30°observed in the diffraction pattern indicate that the synthesized bioglass material might be nanosized. Further, the presence of few sharp peaks along with broad peaks was indicative of semi-crystalline nature of the synthesized material. In the diffraction pattern of the bioglass-ceramic sample, the several typical reflections corresponds to the $(Na_{0.11}Ca_{0.89})(P_{0.11}Si_{0.89})O_3$ phase [JCPDS-46-0163].

The FTIR spectrum of the bioglass sample in the range of 2000-500 cm^{-1} is shown in the Fig. 2. It also depicts the FTIR of the PAMAM dendrimer which was used as a template for the synthesis of BG sample. Within the spectrum of BG, the broad intense peak at 1090 cm^{-1} and a small sharp peak at 467 cm^{-1} are attributed to Si–O–Si asymmetric stretching and bending vibrations respectively. A small shoulder at 963 cm^{-1} is assigned to non-bridging oxygen together with the surface active silanols (Si–OH) groups, which enhances the rate of apatite formation. The peak at 798 cm^{-1} is characteristic ring structures of the silicate network.[38] The peak at 644 cm^{-1} corresponds to P-O bond bending vibration and indicate that phosphate enter as network former. It is to be noted that the characteristic peaks namely -N–H,–C=O and $–NH_3^+$ of PAMAM dendrimer template were not prominently visible and mostly overlapped with the Si-O-Si peaks of BG.

The pore characteristics were evaluated from the nitrogen adsorption-desorption isotherm produced by BET portrayed in Fig. 3(a). N_2 adsorption-desorption isotherm analysis for the sample exhibited IUPAC type IV isotherm pattern with H1 hysteresis. From the pore size distribution (inset in Fig. 3 (a)) graph, presence of multi-sized pores with larger distribution of micropores in the range of 0.5-2 nm diameter, with negligible distribution of mesopores was observed. It is to be noted that a negligible difference in porosity was observed in the lyophilized and pre-heated samples (ESI Fig. S2). It is pertinent to mention that in both the batches during degassing burning of organic fraction was not observed. This was further supported by the obtained TGA graph for the as prepared, lyophilized and pre-heated samples (ESI Fig. S3).

From the TGA graph, it was clearly depicted that upto 130 °C, a 2.5% weight loss was recorded for the as prepared sample, while for the same range of temperature, the pre-heated and lyophilized sample reported <1 % weight loss. This weight loss is attributed to the loss of water molecules adsorbed on the surface of the sample. Thereafter, for the as prepared sample, upto 200 °C, a weight loss of 5% was observed, associated to the chemically absorbed water. For the same range, the pre-heated and lyophilized sample showed negligible weight loss. TGA results validated the fact that no organic fraction burning occurred till 200 °C.

In order to confirm microporous pores distribution of the lyophilized bioglass sample (Fig. 3(a)), BET analysis was extended for t-method and results are displayed in Fig. 3(b). This analysis confirmed the existence of micropores as depicted in inset of Fig. 3(b). Based on the t-method, the surface area was calculated using BJH method is 472 m^2/g.

FESEM analysis (Fig. 4(a,b)) showed that the synthesized bioglass nanoparticles possess spherical like morphology. Furthermore, the EDX results (Fig. 4(c)) confirm that the compositions of these glasses are in good agreement with the theoretical calculations and are listed as a table inset in Fig. 4. The TEM micrograph (Fig. 5(b) further confirmed that the size of the bioglass particles was in the range of 40 to 50 nm and a great number of micropores were visualized inside the nanosized particles after staining with uranyl acetate (Fig. 5 (b)). Irrespective of the two different pre-treatment lyophilization (Fig. 5(b) and pre-heated to 200 °C (ESI Fig. S4), similar morphology was confirmed by TEM analyses. Further, it is interesting to note that the d-spacing value reported in the JCPDS-46-0163 match closely with the experimentally obtained values of selected area electron diffraction (SAED) pattern with the corresponding hkl orientation values as shown in Fig. 5 (as table inset). These observations based on TEM provide an additional support to the existence of $(Na_{0.11}Ca_{0.89})(P_{0.11}Si_{0.89})O_3$ phase which was also indicated by the XRD pattern (Fig. 1).

The density of the as-prepared bioglass-ceramic was measured as 1.9 g/cm^3 which is in close agreement with the density of natural compact bone (1.8–2.2 g/cm^3).[39]

3.2. Plausible nBG synthesis mechanism

PAMAM dendrimers, a starburst hyperbranched polymer are synthesized through stepwise repetitive reaction sequences with ammonia and ethylenediamine forming the initiator core,

initiator layers i.e generations derived from N-(2-aminoethyl) acrylamide and amine group acting as a terminator.[40] It's well known that PAMAM dendrimer is positively charged due to the presence of amino groups on its surface, which acting as a template directs the deposition of the sequentially added precursors. As reported the pK_a values of PAMAM dendrimer's outer shell primary amine is 7-9 and the solution it is taken in has a pH 8, which results in higher positive charge density at the polymer surface.[40] Initially, hydrolysis of TEOS results in the formation of silica which is negatively charged at pH 8 greater than its isoelectric point of 2.[41] This charge attraction results in heterogeneous nucleation of the network formers SiO_2 and P_2O_5, on the surface of the dendrimer. This is followed by the homogenous nucleation of the other precursor molecules. Herein, Na_2O and CaO act as network modifiers by occupying the interstitial sites of the network as reported in the literature[2], in the ionic forms of Na^+ and Ca^{2+} resulting in the conversion of bridging oxygen into non-bridging oxygen i.e. Si-O-Si to Si-O-Na and Si-O-Ca-O-Si formation to balance the network as represented in the schematic diagram (Fig. 6).

In order to elucidate the mechanism of bioglass formation as per the synthetic procedure mentioned above, FTIR spectra of the reaction mixture in the liquid form for each of the sequentially added precursor (namely, TEOS, TEP, Sodium acetate and Calcium acetate) after 30 min interaction on dendrimer template were studied. It is important to mention that differential spectrum was obtained for each of the added precursors in the region from 2000 to 650 cm^{-1} and compared, by subtracting the PAMAM template background from respective spectrum. The detailed discussion on the differential spectrum of the PAMAM interaction with the precursors could be found in ESI S3. The differential spectrum results were further confirmed with CHNSO analysis of the lyophilized BG sample, which indicated the presence of carbon and nitrogen (C = 0.8 w % and N = 0.4 w%). Such an interesting role of templates in the formation of ZnO by bioinspired route was already proven.[28]

The final product acquires a polygonal morphology as evident by the TEM micrographs (Fig. 5). It is supported by the fact that the dendrimer uptill generation 3 is non-spherical in shape, after which they start acquiring spherical shape as reported by Tomalia *et al*.[30] Microporosity is attributed to the space present in the dendrimer structure. These results are in good agreement with the reported ceramic oxide synthesis where the template directs the morphology of the material.[32]

3.3. *In vitro* bioactivity

Bioactivity is defined as the ability of the material to interact with the living tissue by forming a layer whose constituent is similar to the living body. *In-vitro* evaluation of the bioactive nature of the bioglass is performed by the immersion of the material in SBF whose ionic composition and concentration is similar to human blood plasma. If the material is bioactive, then it is expected to form hydroxyapatite layer, one of the major constituent of the bone mineral. To examine the *in vitro* apatite layer formation on the surface of the pelletized BG sample, sequential monitoring was carried out by XRD, FTIR and FESEM. Additionally, changes in the chemical composition of the counterpart of the BG pellet i.e. the ion concentration of the SBF solution after immersion of the samples as a function of time were evaluated by ICP-AES technique and simultaneously pH changes were also measured.

Fig. 7 illustrates the XRD pattern obtained before and after interaction of BIS-nBG-DG3 with SBF at various timings. Interestingly after 24 hours of BG interaction with SBF solution, a disappearance in the XRD peak pattern corresponding to the BIS-nBG-DG3 nanocrystals (Fig. 7) was observed and there appeared a broad hump, which indicates that the deposited material is amorphous in nature. The observed change in the XRD pattern indicates the rearrangement in the local atomic structure of the glass-ceramic sample after incubation with SBF. Thereafter, 15 days of interaction with SBF shows (Fig. 7) appearance of few sharp peaks in the 2θ range of 30.23° to 32.56°, indicative of switching of the deposited material on the BG surface from amorphous to crystalline phase and in good agreement with earlier reports.[42,43] The XRD peaks sharpness of the 15 days incubated sample was found to be improved. Several typical reflections corresponding to hydroxyapatite phase ($Ca_{10}(PO_4)_6(OH)_2$) (JCDS 09-0432) were observed in the BG sample interacted with SBF for 30 days, which reveals the formation of hydroxyapatite in the crystalline phase.

Further, the formation of hydroxyapatite was confirmed by observing the presence of characteristics vibration modes of phosphates and carbonates in the FTIR spectra (Fig. 8) of samples immersed in SBF. Interestingly, after immersing the glass samples into SBF for 24 h, a peak at 1644 cm^{-1} corresponding to hydroxyl group for the deposited sample was observed. Apart from this, the appearance of new peaks corresponding to carbonate (small sharp peak at

1449, 1554, 864 and 802 cm^{-1}) and phosphate group absorption bands with a sharp peak at 1073 cm^{-1} containing a shoulder at 1198 cm^{-1} and peak at 962 and 558 cm^{-1} were recorded. However, as the interaction time was increased to 15 days, compared to 1 day interaction a broad peak was observed at 1094 cm^{-1} and small peaks at 1219, 955 cm^{-1} and sharp peak at 551 cm^{-1} were observed corresponding to phosphate group. Interestingly, a sharp new peak was visualized in the spectrum at 1644, 1387 and 794 cm^{-1} in addition to the peaks at 1553, 1449 cm^{-1} corresponding to the carbonate group. It is pertinent to mention that the sharpness of the peaks further enhanced as the interaction time was increased to 30 days. A noticeable doublet at 1100 cm^{-1} and 1038 cm^{-1} as well as peaks at 962 (a weak shoulder), 600 and 563 cm^{-1} corresponding to phosphate group and the appearance of new peaks corresponding to carbonate at 1484 to 1400 cm^{-1} with the decrease in the peak sharpness at 1449, 1554, 878 and 802 cm^{-1} were observed which are in good agreement with the characteristic vibrational bands of the carbonated hydroxyapatite (HCA) phase. The presence of phosphate, carbonate and hydroxyl group indicates that the formed hydroxyapatite was carbonated hydroxyapatite.[44]It is also noteworthy that an increase in interaction time of the glass-ceramic sample with SBF causes the intensity of the phosphate peaks to increase, which indicates the formation of an apatite-rich layer on the glass surface. It is worthwhile to note the peak at 798 cm^{-1}, a characteristic peak for the ring structure of the silicate network[44] disappear gradually, only a trace was observed for the 30 days old sample. This disappearance validates the dissolution of ions on the BG surface facilitating the conversion of silicate to silanol groups as per the bioactivity mechanism proposed by Hench.[45]

After soaking in SBF, the surface of the bioglass was examined through FESEM and micrographs corresponding to 1, 15 and 30 days are displayed in Fig. 9. For a comparative purpose, FESEM micrograph corresponding to 0 day interaction displayed in Fig. 4 has been considered. After 1 day interaction with SBF buffer, hydroxyapatite nodules were observed to appear (Fig. 9 (a)). Interestingly, these newly formed hydroxyapatite nodules on further immersion in SBF were aggregated together and distributed throughout the surface of the bioglass material as visualized in the micrographs corresponding to 15 (Fig. 9 (b)) and 30 days (Fig. 9 (c)) respectively. Based on the monitored XRD (Fig. 7) pattern as well as FTIR (Fig. 8) spectrum, the observed material deposition on the surface of the BIS-nBG-DG3 after interaction

with SBF could be attributed to the bone-like HCA layer formation in a good agreement with the literature.[29,42,44]

The hydroxyapatite layer developed in SBF has been called bone-like apatite, because of its composition and structure similar to those of bone mineral rather than of sintered stoichiometric apatite. The bar chart depicted in Fig. 9 represents the atomic percentage of Ca and P quantified from microchemical analysis by EDX method. The bar chart reveals a notable increase in Ca and P content after 30 days interaction with SBF, which additionally support the deposition of hydroxyapatite layer over virgin bioglass. Additionally, the zeta potential of the as prepared sample in TRIZMA buffer at pH 8 was determined to be -40.6mV (Figure not shown). It is pertinent to mention that the negatively charged surface promotes growth of bone-like apatite on the bioactive glass surface as reported by Kokubo *et al*.[46]

During bioactivity test, ionic dissolution rate of Si, P, Na and Ca with time was monitored in the counterpart of the BG pellet i.e. SBF solution using ICP-AES with the simultaneous record of pH values (Fig. 10). In our study, an increase in the dissolution rate of metal ions in the order of Na, Ca, P and Si were observed. Correspondingly, a gradual increase in the pH value of the surrounding medium was determined to rise from pH 7.2 to pH 8.2 upto 15 days, there after it attains saturation. Initially a steep rise in pH value with time was observed due to fast ion exchange processes on the glass surface. Cations such as Na^+ and Ca^{2+} near the glass surface get exchanged for H_3O^+ or H^+ from the surrounding medium, which raises the pH value of the SBF solution. This rapid increase in pH is followed by hydrolysis of silica group creating silanols which favor pH rise. Thereafter, a continuous silanol formation at the glass interface occurs followed by condensation and repolymerization of SiO_2 rich layer on the surface that exhaust Na and Ca cations. Subsequently, the pH of the solution remains constant due to the rapid growth of apatite phase that overcomes the release rate of ions into the solution.[47] It is noteworthy that the observed high pH values are in good agreement with the earlier reported data.

The increase in pH values results in decreasing the solubility of the hydroxyapatite and thus assist in the precipitation process. Apart from this, faster kinetic deposition process of hydroxyapatite is expected to be obtained by using nanoparticles as small particle size and high

specific surface area of 472 m^2/g of the sample increases its contact area with the fluid, which accelerate the biodegradation of the sample as per Lei *et al*.[8]

3.4. Evaluation of Biocompatibility/cytotoxicity

Nanoscale bioactive glass has been proved to provide improved surface properties and apatite forming ability.[7] However, their biocompatibility is still a matter of concern for tissue regeneration application. The cell cytotoxicity of the biomaterial was evaluated using MTT assay after 48 h interaction time and the ressults are displayed in Fig. 11. Herein, human osteoblast-like osteosarcoma cells (U2OS) grown in DMEM medium was considered as a positive control and the medium in the absence of cell was taken as negative control. It is interesting to note that in the presence of PAMAM dendrimer templated bioglass extract, nearly 99% cells were alive. The difference between the cell growth in the absence and presence of BG sample was about 1% and these results are in good agreement with the earlier findings.[47-49] The optical micrographs of the osteosarcoma cells before and after contact with the bioglass showed similar morphologies (Figure not shown), which supports the good cytocompatibility of the BIS-nBG-DG3. It is pertinent to mention that suitability of the bioglass sample for cell spreading was examined by growing osteosarcoma cells directly onto a bioactive glass pellet for 24 h, 48 h and 6 days and FESEM micrographs are portrayed in Fig. 12.

The FESEM images reveal that the normal morphological phenotype of cells attaches on the surface of the PAMAM dendrimer templated bioglass pellet, further evidencing the cytocompatibility of the bioactive material. Interestingly, low cell adherence is observed on sample on day 1, with the gradual increase in cell spreading on day 2, followed by appreciable cell proliferation clearly observed over the surface of the bioglass pellet that was subjected to 6 days culture. It is envisaged that osteoconductive hydroxyapatite layer is formed on the surface of the bioglass sample immersed in DMEM media[1] which is sensed by the cells for proper attachment to the surface of the sample and contributed to the cell proliferation. Hydroxyapatite nodules (HNO) were observed which were closely surrounded by cellular protrusions as reported by Wang *et al*.[50] Biological apatite formation on the surface of the bioglass stabilizes the bioactive Si release which is critical for the bone-related cell proliferation and differentiation.[51,52] It is pertinent to mention that the surface properties such as topography, roughness, surface area

and charge play a critical role in cell adherence and proliferation. It is likely that surface roughness is related to the availability of the medium and serum proteins through the grooves underneath the attached cells, as proposed by Deligianni *et al*.[53] Cell fingers is the another salient feature that enhances the extent of cell spreading. It is expected that cells with fingers longer than 10 micrometer results in complete spreading because all of its individual cells have fingers longer than 10 micrometer (Fig. 12). Moreover, high specific surface area enhances the cell adherence. It is evident through such a visualization of active attachment of cells to the sample surface by membranous processes that the synthesized material is cytocompatible and could lead to proper tissue growth.

3.5. Evaluation of the mechanical stiffness

Apart from providing improved features on the material surface, nanoscale bioactive glass also assists in improving the mechanical property of the material. The mechanical stiffness of the as-prepared bioglass material was evaluated using dynamic mechanical analyzer (DMA). The obtained results are portrayed in Fig. 13. Herein, DMA experiments were carried out based on frequency scan to monitor the variations of the viscoelastic properties of the sample upon immersion in SBF. A small increase in storage modulus (E') with respect to increasing frequency was observed for both, before and after 30 days interaction with SBF, with the increase profiles being more or less same for both the samples as shown in Fig. 13 (right panel).

For the previously immersed sample in SBF, comparatively a higher value of E' is observed confirming the induction of stiffness in the sample after immersion in SBF due to the development of an apatite layer over the sample surface. Caridade *et al*[34] also demonstrated that the stiffness of the material increases after SBF immersion. Since the synthesized sample was of nano-dimension, it is speculated that the larger surface area results in faster kinetics and large carbonated hydroxyapatite deposition leading to high load transfer ability and stiffness of the apatite layer. This increase in stiffness of the material after immersion is also expected due to the presence of crystalline phase in the 30 days SBF interacted sample as revealed by XRD pattern (Fig. 7).

The loss factor (as a measure of mechanical damping property) is defined as the ratio of the amount of energy dissipated by viscous mechanisms with respect to energy stored in the elastic

component, thus provides information about the damping properties of the material. In general, it is observed that the value of tan δ decreases with the increase in the frequency (Fig. 13 (left panel)) suggesting that the material's damping property was improved by becoming less viscous and more elastic. The nano nature of the material indicates its higher capacity to dissipate mechanical energy. This property will help in preventing the breaking of bone bonding material. In this way, BG can act as an impact modifier. It is therefore expected that not only does the formed surface hydroxycarbonate apatite layer bond strongly to the substrate, but would also provide an effective uniform gradient of stress transfer from bone to implant.[54] Possession of such an interesting mechanical damping property makes it a superior material of choice for bone-joint replacement then our earlier reported CT-DNA based bioglass though bio-inspired route.[29]

3.6. Focus on the advanced application of Bioglass

As shown earlier in our findings under section 3.1 and 3.5, we were successful in synthesizing a mechanically strong implant material with superior textural properties (Fig. 3, 5). In addition to this, observed cytotoxicities and cell proliferation (Fig. 11, 12), encouraged us to study the application of the nanobioactive glass material as a carrier vector for therapeutic gene. It is pertinent to remember that free nucleotides and DNA are rapidly degraded by serum nucleases in the blood when injected intravenously thus many research groups currently focuses on designing effective carrier vectors that can compact and protect therapeutic nucleotide for gene delivery.[55]

For any material to function as a gene carrier, it's a pre-requisite for the material to be able to condense the required gene. For the same requirement, the material needs to be positively charged. Positively charged BG material was achieved through amination. The observed zeta potential after amination was +30 mV (Figure not shown). The FTIR and TEM of the aminated nanoparticle are discussed as follows. -N-H and -Si-N-H bond vibrational peaks were observed in the recorded FTIR spectra, indicating the successful amination of the material. TEM microimage showed no change in the textural property. FTIR spectra (ESI Fig.S7) and TEM (ESI Fig. S8) for the aminated bioglass (ABG) are shown in the supplementary.

In order to study the DNA-cationic ligand interaction, *in vitro* studies based on gel condensation assay, CD and UV-melting has been successfully carried out by numerous researchers using various other vectors.[35,36] Similar i*n-vitro* studies were performed on bioglass nanoparticle-

pDNA interacted complex. In addition to this AFM was also recorded to visualize the pDNA compaction by aminated BG nanoparticles.

Gel condensation assay: Gel electrophoresis helps to assess the interaction between DNA and oppositely charged BG nanoparticle. Partial or full neutralization of the negative charges on DNA occurs upon its association with the positively charged BG nanoparticle. Thereby, the migration of DNA through the gel is slowed down or almost completely hindered.

Gel electrophoresis studies were performed on the pDNA before and after complexation with the positively charged BG nanoparticle under investigation at the weight ratio of (pDNA:ABG) 1:0,1:10,1:20,1:30,1:40,1:50,1:60,1:70,1:80,1:90 and 1:100 (µg:µg), and the images are portrayed in Fig. 14(a). The first well of the agarose gel electrophoresis depicts the migration of free pDNA. Subsequently, smearing and a gradual decrease in the intensity as well as mobility of the bands were observed as the weight ratio of pDNA: aminated BG was increased upto 1:30, which indicates a reduced amount of pDNA in the bands due to their interaction with the positively charged BG. It also indicates towards the coexistence of free pDNA and pDNA:ABG complexes. Thereafter, for the weight ratios above 1:30, the migration of pDNA was not visible, suggesting for the highly cooperative interaction between the pDNA and positively charged BG. Thus all pDNA molecules were complexed with the BG nanoparticles. Interestingly, prominently visible retarted DNA is seen at the wells for weight ratios above 1:30 indicating complete neutralization of DNA by the nanoparticles.

Circular dichroism (CD): Conformational changes in the double helix of DNA induced by the binding of ligands are detected by CD spectra. This helps in monitoring the secondary structural changes due to the pDNA:ABG nanoparticle complex formation. It is well known that, B-conformation of DNA produces two characteristics CD signals: a positive peak at 275 nm and a negative peak at 245 nm. Fig. 14(b) represents CD spectra of pDNA in the absence and presence of the bioglass nanoparticles under investigation at various weight ratios of 1:0, 1:10, 1:20, and 1:30. For all the experiments, the pDNA amount was maintained at 5µg. From the obtained CD spectra it was evident that the intensity of the positive and negative signal at 275 nm and 245 nm respectively were decreased upon the addition of the ABG nanoparticles, upto the weight ratio of 1:20. Interestingly, CD signal was not observed for the weight ratio 1:30 indicating the complete

compaction of pDNA by the ABG nanoparticles, in fair agreement with the gel condensation assay result.

UV Melting: In order to measure double-helix stability of the pDNA solution in the absence and presence of the aminated bioglass nanoparticles, UV-melting experiments were performed. When a double stranded DNA undergoes denaturation due to the increase in temperature, the base stacking is disrupted, which leads to the increase of the absorbance at 260 nm. The temperature at the midpoint of the transition is known as the melting temperature (T_m), which gives a good indication of the stability of the double helix. Fig. 14(c) shows the characteristic melting profiles of free pDNA and its complexes with the ABG nanoparticle under study. As expected, the free pDNA solution showed a monophasic melting behavior with a melting temperature around 75 °C. When the weight ratio of the pDNA:ABG was increased, an increase in the melting point was observed with the retention of the general melting profile of pDNA. These data closely correlate with the gel electrophoresis data. As the ABG binding affinity increases, a change in T_m can be seen for corresponding complexes with the mobility shift as seen in the gel study.

AFM: pDNA was visualized under AFM, both before and after interaction with the ABG nanoparticles of weight ratio 1:0, 1:10 and 1:30. As noticed through earlier experimental results (Fig. 14 (a,b,c)), complete compaction has been visualized for the weight ratio 1: 30 (Fig. 14(d)).

Transfection Studies: Only the DNA compaction ability of any material is not enough until it could be utilized as a carrier for transfection. In view of this, cellular uptake capability of the pDNA compacted ABG was further studied. As it is a known fact that compacted complexes at low weigh ratios need not be feasible for transfection so the different weight ratios of 1:50, 1:100, 1:125, 1:150, 1:175 of pDNA:ABG complexes were chosen to study the cellular uptake of the pDNA:ABG complex. The cellular uptake of the complexes was evaluated through luciferase assay while the cell morphology was observed through microscopic analysis. Interestingly normal cell morphology was retained as observed through microscopic analysis after 24 h (Fig.15) of interaction of CHO-K1 cell line and pDNA:ABG complex. The luciferase assay results reflect that crystallinity and microporous nature of the material plays a critical role in the cellular uptake of the pDNA. Unlike the literature reported observation of the reduction in DNA

dosage availability for cellular uptake due to collapse in the porous structure of the gene carrier[56], herein the crystalline nature of the bioglass nanoparticles prevents the collapse of the microporous structure in media. It is pertinent to recall that the slow dissolution characteristics of the partially crystalline bioglass material in SBF is well known as compared to the amorphous BG.[57] As shown in figure 15, the pDNA:ABG complex showed the 4 to 5 orders of transfection efficiency in all the weight ratios with highest at 1:125 ratio, which shows 6 orders of transfection efficiency. Since effect of surface area on the distribution of the pDNA is widely known, an increased surface area can maximize the number of cells that contact pDNA:ABG complex that is releasing the pDNA. These results confirm application of the bioglass nanoparticle as a suitable nanocarrier for gene delivery applications apart from bone regeneration.

4. Conclusion

In the present study, we have synthesized the microporous monodispersed multifunctional bioactive glass nanoparticles through biologically inspired route using PAMAM dendrimer as a template. Bio-inspired method promises good morphological control in an eco-friendly and cost effective manner. The synthesized nanocrystalline bioglass with higher surface area and excellent bioactivity is more suitable to replace the mechanical function of damaged bone until sufficient new bone tissue has formed with good load transfer ability. In particular, it is worth noting that a good proliferation of osteoblast like osteosarcoma cells over the bioglass surface and 99% cell viability as reported by MTT assay confirms the excellent biocompatibility of the nanosized microporous bioglass particles. The as prepared microporous, monodispersed, nanocrystalline PAMAM dendrimer templated bioglass possessing good damping property facilitates its application in bone regeneration. More importantly, in addition to bone regeneration, the characteristic nanodimension of the bioglass material extends its application in the field of non-viral gene delivery applications.

Acknowledgement

Financial support for this work (DST fast track project SR/FT/CS-77/2010) from the Department of Science and Technology, Government of India, New Delhi, is gratefully acknowledged. The authors acknowledge Dr. Munia Ganguli and co-worker, Poornemaa Natarajan, IGIB Delhi for

lending the lab facility for carrying out cell-interface study; support from Ms Hema Kumari Alajangi of DTU for assisting in cell culture work; Mr. AmanVerma of DTU in mechanical measurement; Dr. Gajender Saini of AIRF, JNU for TEM recording; SMITA-lab, IITD for FESEM facility. Special thanks to Mr. Anil Kumar of Physics and Astrophysics, DU for the experimental support from time to time.

References

1. Q. Chen, C. Zhu, and G. A. Thouas, *Progress in Biomaterials* 2012, **1**, 1-22.
2. J. R. Jones, *ActaBiomaterialia* 2013, **9**, 4457–4486.
3. V. M. Pacheco, L. L. Hench and A. R. Boccaccini, *ActaBiomaterialia* 2015, **13**, 1–15.
4. T. Kokubo, H. M. Kim and M. Kawashita, *Biomaterials* 2003, **24**, 2161–2175.
5. E. Palin, H. N. Liu and T. J. Webster, *Nanotechnology* 2005, **16**, 1828–1835.
6. A. A. R. de Oliveira, D. A. de Souza, L. L.S. Dias, S.M. de Carvalho, H. S. Mansur and M. de Magalhaes Pereira, *Biomed. Mater.* 2013, **8**, 025011-025025.
7. P. A. Tran, L. Sarin, R. H. Hurt and T. J. Webster, *J.Mater. Chem.* 2009, **19**, 2653-2659.
8. B. Lei, X. Chen, X. Han and J. Zhou, *J. Mater. Chem.* 2012, **22**, 16906-16913.
9. C. Wu, W. Fan and J. Chang, *J. Mater. Chem. B* 2013, **1**, 2710-2718.
10. F. Quintero, J. Pou, R. Comesan, F. Lusquin, A. Riveiro, A. B. Mann, R. G. Hill, Z. Y. Wu and J. R. Jones, *Adv. Funct. Mater.* 2009, **19**, 3084–3090.
11. T. J. Brunner, R. N. Grass and W. J. Stark, *Chem. Commun.* 2006, 1384-1386.
12. S. K. Misra, D. Mohn, T. J. Brunner, W. J. Stark, S. E. I. Roy, V. Salih, J. C. Knowles and A. R. Boccaccini, *Biomaterials* 2008, **29**, 1750-1761.
13. P. Sepulveda, J. R. Jones and L. L. Hench, *J. Biomed. Mater. Res.* 2002, **61**, 301-311.
14. M. V. Regi, C. V. Ragel and A. J. Salinas, *Eur. J. Inorg. Chem.* 2003, **2003**, 1029-1042.

15. T. J. Webster, C. Ergun, R. H. Doremus, R. W. Siegel and R. Bizios, *J. Biomed. Mater. Res.* 2000, **51**, 475-483.

16. T. J. Webster, R. W. Siegel and R. Bizios, *Biomaterials* 1999, **20**, 1221-1227.

17. L. M. Mukundan, R. Nirmal, D. Vaikkath and P. D. Nair, *Biomatter* 2013,**3**,e-24288 (1-10).

18. A. El-Fiqi, T. H. Kim, M. Kim, M. Eltohamy, J. E. Won, E. J. Lee and H. W. Kim, *Nanoscale* 2012, **4**, 7475-7488.

19. S. Lin, W. Van den Bergh, S. Baker, and J. R. Jones, *ActaBiomater* 2011, **7**, 3606-3615.

20. J. Hum and A. R. Boccaccini, *J Mater Sci: Mater Med* 2012, **23**, 2317–2333.

21. G. Blackburn, T. G. Scott, I. S. Bayer, A. Ghosh, A. S. Biris and A. Biswas, *J Mater Chem B* 2013, **1**, 1519-1534.

22. M.A. Mintzer and E.E. Simanek, Nonviral vectors for gene delivery, *Chem. Rev.* 2009, **109**, 259–302.

23. X. Li, X. Chen, G. Miao, H. Liu, C. Mao, G. Yuan, Q. Liang, X. Shen, C. Ning and X. Fu, J. Mater. Chem. B, 2014, **2**, 7045–7054.

24. G. Jell and M. M. Stevens, *J Mater Sci: Mater Med* 2006, **17**, 997–1002.

25. H. Cölfen and S. Mann, *Angew. Chem. Int. Ed.* 2003, **42**, 2350–2365.

26. P. M. Ajayan, L. S. Schadler and P. V. Braun, Nanocomposite Science and Technology, *Wiley-VCH VerlagGmb H Co. kGaA*, Weinheim 2003, ISBN: 3-527-30359-6.

27. P. Atanasova, R. T. Weitz, P. Gerstel, V. Srot, P. Kopold, P. A. V Aken, M. Burghard and J. Bill, *Nanotechnology* 2009, **20**, 365302-365309.

28. L. P. Bauermann, A. del Campo, J. Bill and F. Aldinger, *Chem. Mater.* 2006, **18**, 2016-2020.

29. D. Santhiya, H. K. Alajangi, F. Anjum, S. Murugavel and M. Ganguli, *J. Mater. Chem. B* 2013,**1**, 6329-6338.

30. D. A. Tomalia, A. M. Naylor and W. A. Goddard III, *Angew. Chem. Int. Ed. Engl.* 1990, **29**, 138-175.

31. M. F. Ottaviani, S. Bossmann, N. J. Turro and D. A. Tomalia, *J. Am. Chem. Soc.* 1994, **116**, 661-671.

32. F. Zhang, S. P. Yang, H. M. Chen, Z. H. Wang and X. B. Yu, *J of Cryst Growth* 2004, **267**, 569-573.

33. T. Kokubo, *Biomaterials* 1991, **12**, 155–163.

34. S. G. Caridade, E. G. Merino, N. M. Alves, V. Z. Bermudez, A. R. Boccaccini and J. F. Mano, *Journal of the mechanical behavior of biomedical materials* 2013, **20**, 173–183.

35. V. Jadhav, S. Maiti, A. Dasgupta, P. K. Das, R. S. Dias, M. G. Miguel, and B. Lindman, *Biomacromolecules*, 2008, **9**, 1852–1859.

36. D. Santhiya, R. S. Dias, A. Shome, P. K. Das, M. G. Miguel, B. Lindman and S. Maiti, *Langmuir* 2009, **25**, 13770-13775.

37. S.T.M. Allard, K. Kopish and Promega Co, *Cell Notes* 2008, 23-26.

38. A. S. Herman, Infrared Hand Book, Plenum, New York, 1963.

39. M. Peter, N. S. Binulal, S. V. Nair, N. Selvamurugan, H. Tamura and R. Jayakumar, *Chem. Eng.* J. 2010, **158**, 353-361.

40. D. A. Tomalia, H. Baker, J. Dewald, M. Hall, G. Kallos, S. Martin, J. Roeck, J. Ryder and P. Smith, *Polymer Journal* 1985, **17**,117-132.

41. S. Schwarz, K. Lunkwitz, B. Kessler, U. Spiegler, E. Killmann and W. Jaeger, *Colloid Surf.* A 2000, **163**, 17-27.

42. C. Vaid, S. Murugavel, R. Kashayap and R. P. Tandon, *Microporous and Mesoporous Materials* 2012, **159**, 17–23.

43. W. Huang, D. E. Day, K. Kittiratanapiboon and M. N. Rahaman, *J Mater Sci Mater Med* 2006, **17**, 583–596.

44. B. Lei, X. Chen, Y. Wang, N. Zhao, C. Du and L. Fang, *J. Am. Ceram. Soc*. 2010, **93**, 32-35.

45. L. L. Hench, *J. Am. Gram. Soc.* 1991**, 74**, 1487-1510.

46. T. Kokubo, H. M. Kim, M. Kawashita and T. Nakamura, *J. Mater. Sci.: Mater. Med.* 2004**, 15**, 99–107.

47. A. Martinez, I. Izquierdo-barba and M. Vallet-Regi, *Chem. Mater.* 2000**, 12,** 3080-3088.

48. T. Kokubo, F. Miyaji, H. M. Kim and T. Nakamura, *J. Am. Ceram. Soc.*1996**, 79**, 1127–1129.

49. L. L. Hench, J. Wilson and D. C. Greenspan, *J. Aust. Ceram. Soc.* 2004**, 40**, 1–42.

50. H. Wang, H. C. Schröder, B. D. Seifert, K. Kropf, U. Schlossmacher, M. Wiens and W. E. G. Müller, *J. Tissue. Eng. Regen. Med.* 2013**, 7**, 767–776.

51. B. Lei, X. Chen, X. Han and Z. Li, *J. Mater. Chem.* 2011**, 21**, 12725-12734.

52. A. Hoppe, N. S. Guldal and A. R. Boccaccini, *Biomaterials* 2011**,32**, 2757-2774.

53. D. D. Deligianni, N. D. Katsala, P.G. Koutsoukos and Y. F. Missirlis, *Biomaterials* 2001, **22**, 87-96.

54. W. R. Lacefield, Hydroxyapatite coating In: *An Introduction to Bioceramics* L. L. Hench and J. Wilson (eds.), World Science, Singapore 1993,223-238.

55. M. A. Mintzer and E. E. Simanek, *Chem. Rev.* 2009,**109**, 259–302.

56. J. H. Jang and L. D. Shea, *Journal of Controlled Release* 2003, **86**, 157–168.

57. O. Peitl, G.P. LaTorre and L.L. Hench, *J Biomed Mater Res* 1996, **30**, 509–514.

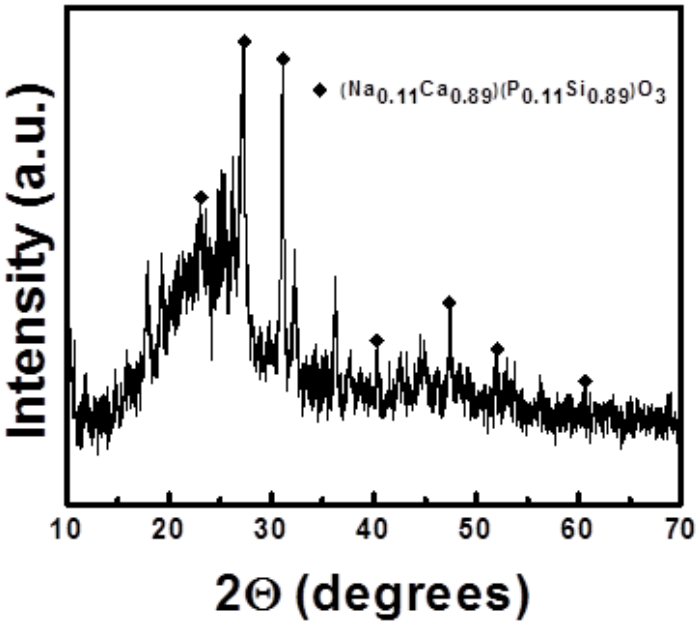

Fig. 1. Wide angle XRD pattern of BIS-nBG-DG3.

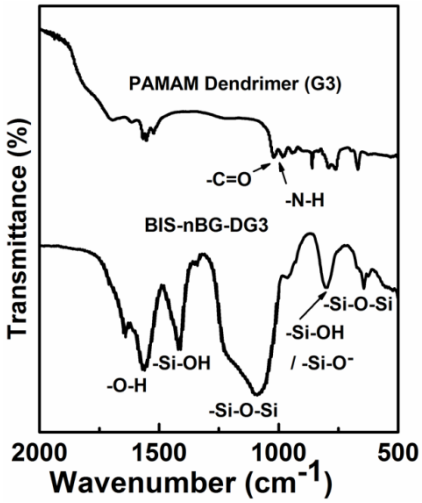

Fig. 2. FTIR spectra of PAMAM dendrimer (G3) and BIS-nBG-DG3.

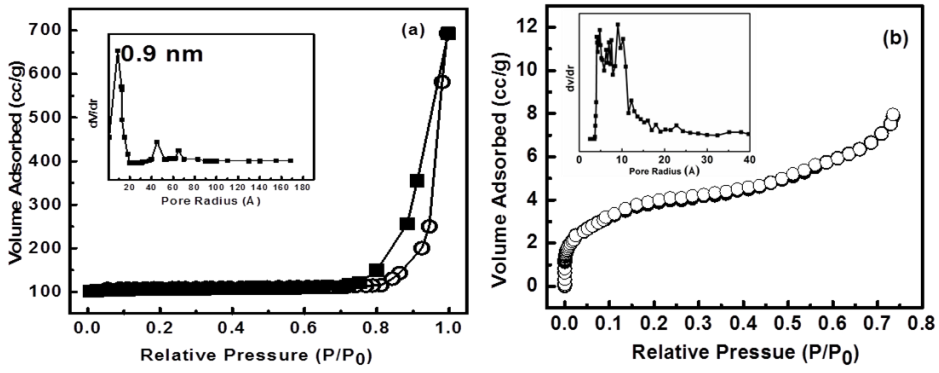

Fig. 3. Nitrogen adsorption–desorption isotherm and pore size distribution (inset) of BIS-nBG-DG3 glass-ceramic sample: (a) normal method and (b) t-method of analysis.

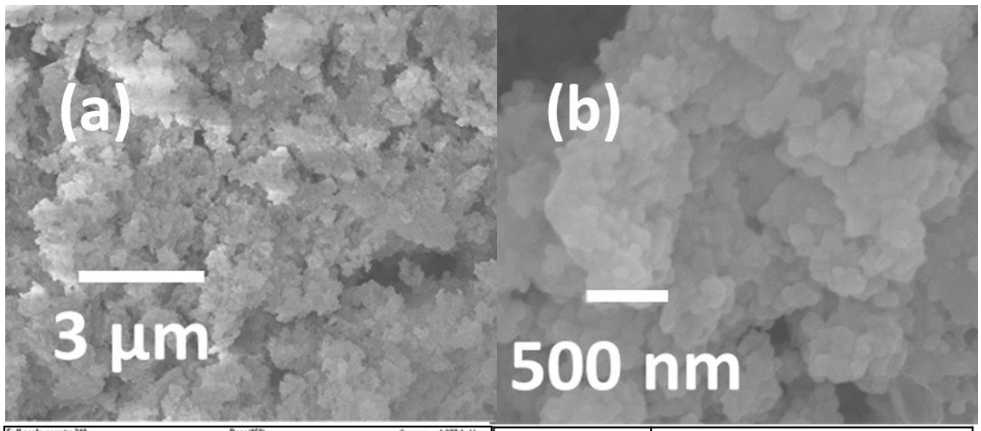

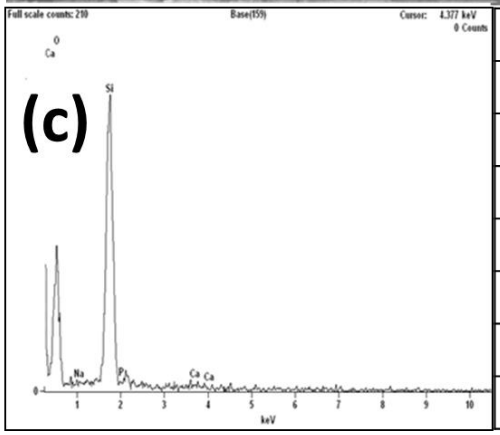

Element	Atomic %	
	Observed	Calculated
Si	15.35	15.38
O	54.49	54.13
Na	15.20	16.23
Ca	14.46	13.46
P	0.50	0.74
Total	100	99.94

Fig. 4. FESEM micrographs showing surface morphology at different magnification (a) 25000 X and (b) 100000 X (c) EDX spectra and table represents elemental analysis of BIS-nBG-DG3.

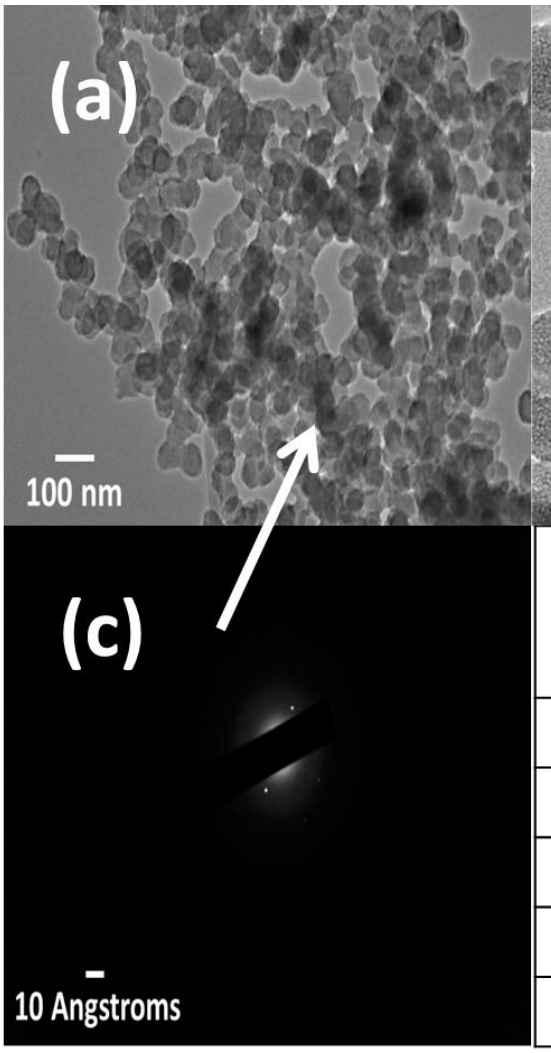

d-value (Å) (SAED)	d-value (Å) (JCPDS)	hkl value
1.86	1.87	$3\bar{3}1$
2.72	2.72	121
2.89	2.88	$\bar{1}\bar{1}2$
3.19	3.10	210
3.78	3.88	200

Fig. 5. a) TEM image of as prepared BIS-nBG-DG3 at the magnification of 20 KX along with SAED pattern (c). (b) TEM image of BIS-nBG-DG3 after uranyl acetate staining at 29 KX. The table represents the d values comparison based on SAED and JCPDS corresponding to which hkl orientation value is mentioned (JCPDS-46-0163).

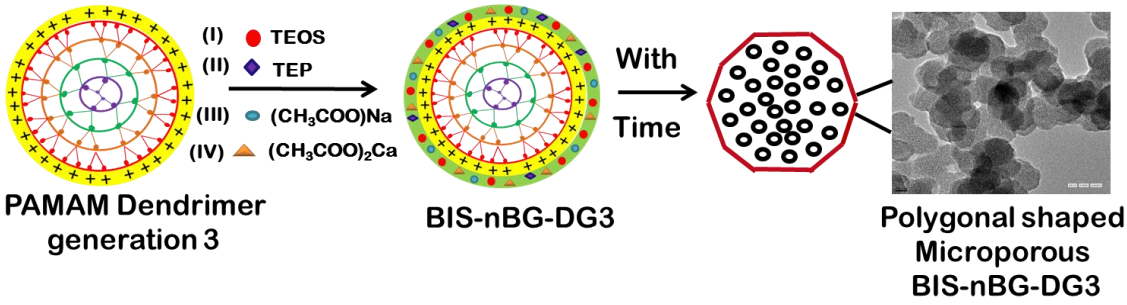

Fig. 6. Schematic representation of nBG synthesis mechanism. Color coding for the image of PAMAM dendrimer generation 3: purple, core cell (G = 0); green, initiator cells (G = 1); brown, interior cells (G = 2); red, surface cells (G = 3).

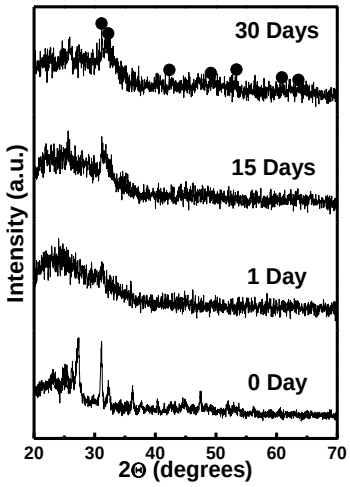

Fig. 7. XRD pattern of BIS-nBG-DG3 before and after interaction with SBF at various immersion timings.

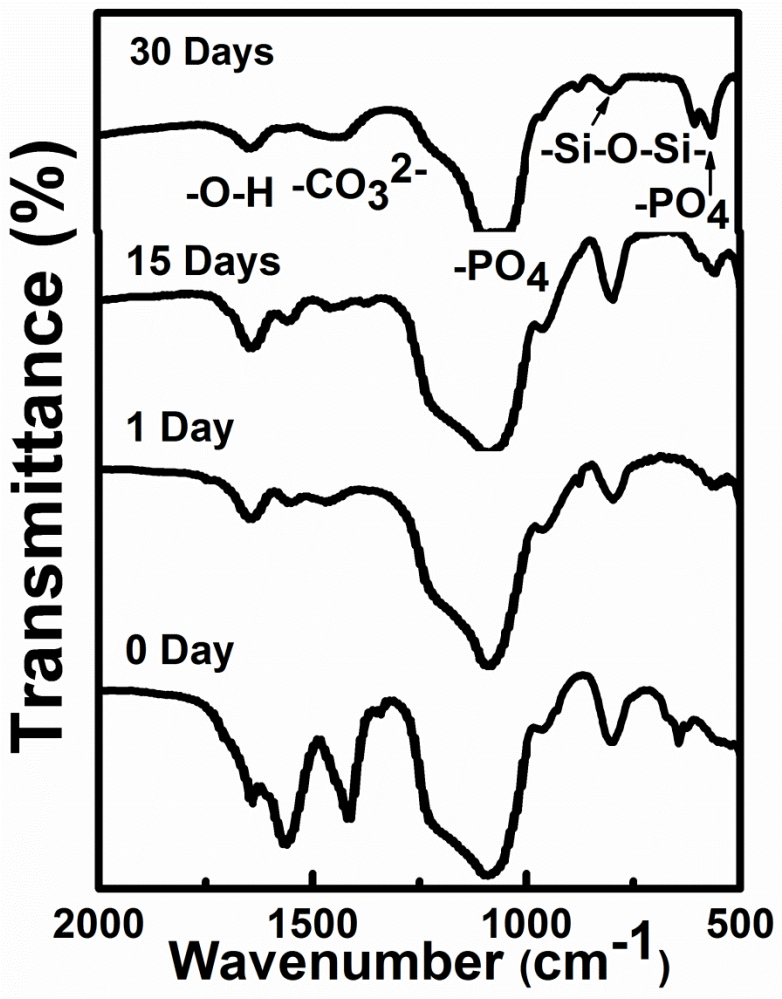

Fig. 8. FTIR spectra of BIS-nBG-DG3 before and after interaction with SBF at various immersion timings.

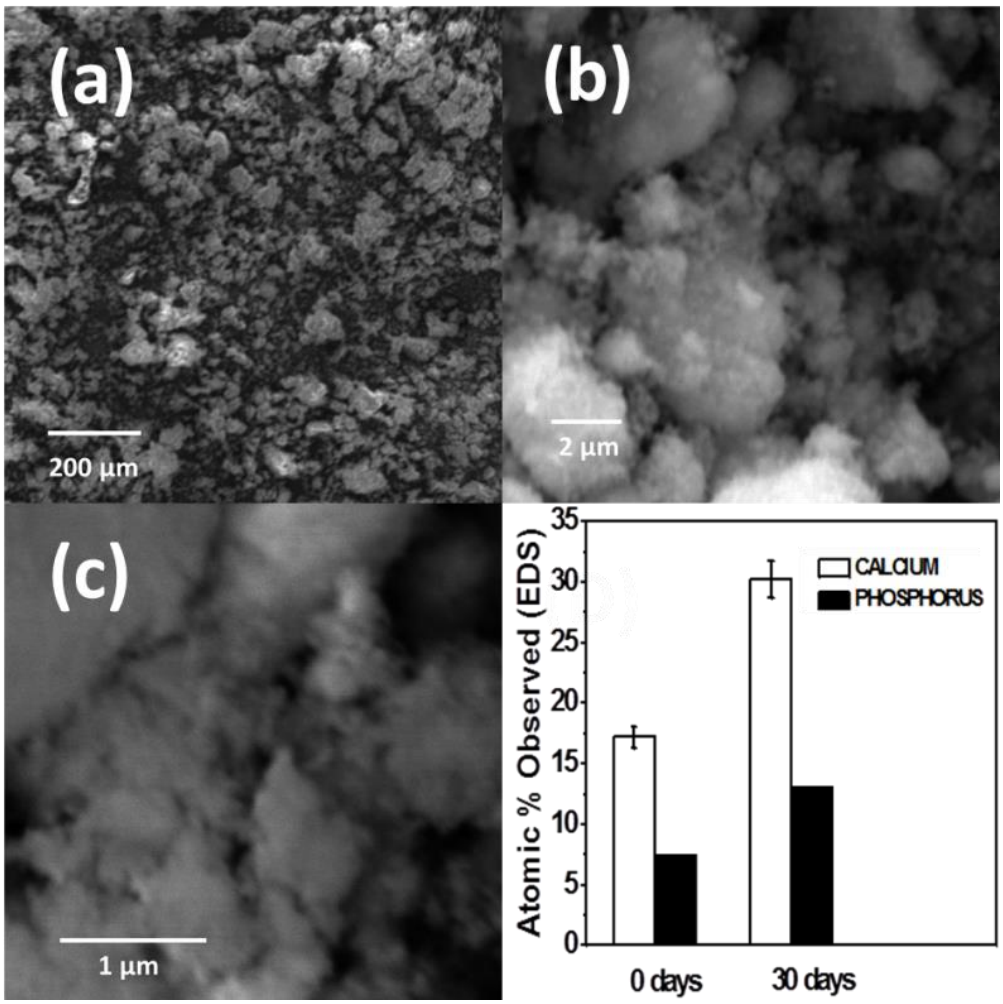

Fig. 9. FESEM micrographs showing surface morphology of bioglass BIS-nBG-DG3 after immersion in SBF at (a) 1 day, (b) 15 days, (c) 30 days at various magnification of 126X, 40.2 KX and 9.36 KX respectively. Graph represents the atomic % of calcium and phosphorus of BIS-BG-D0 surface before and after exposing to SBF solution (as observed by EDS).

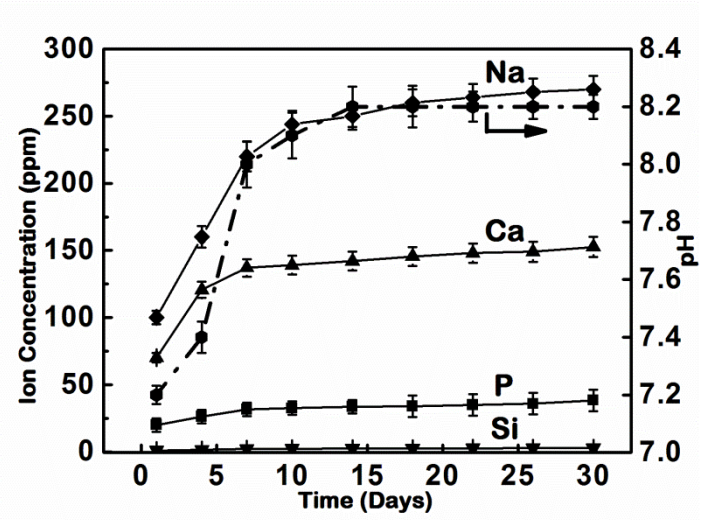

Fig. 10. The variation of pH values of the solution (SBF) as a function of soaking time (Right axis) and an elemental analysis of Na, Ca, P and Si ion concentrations before and after interaction of BIS-nBG-DG3 with SBF at different intervals of time.

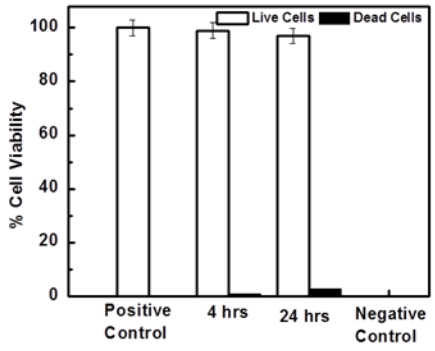

Fig. 11. MTT assay demonstrating biocompatibility of BIS-nBG-DG3.

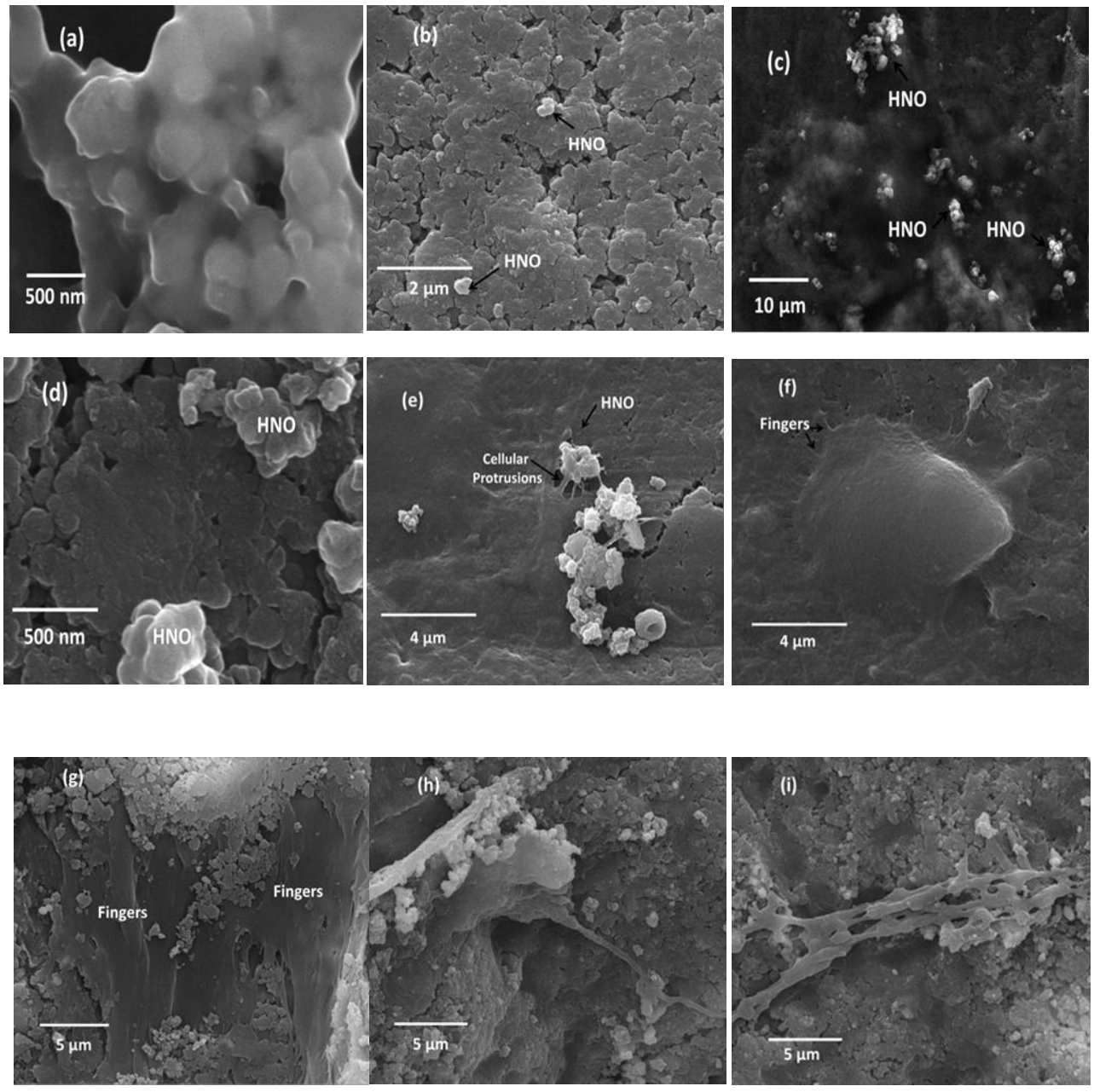

Fig. 12. FESEM images of U2OS cells cultured in DMEM media on BIS-nBG-DG3 pellet for (b-c) 1 day (d-f) 2 days and (g-i) 6 days. (a) Represents the negative control. Images were recorded at various magnifications of (a) 58.3 KX (b) 40 KX (c) 2.89 KX (d) 85.7 KX (e-f) 20 KX (g-i) 12 KX. HNO: Hydroxyapatite nodules.

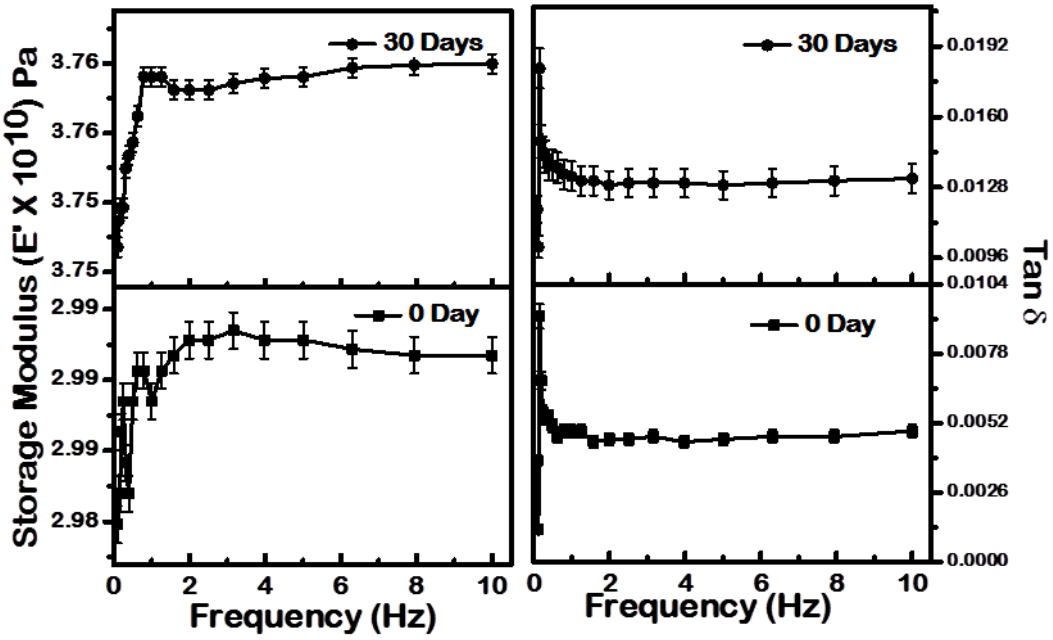

Fig. 13. Comparison of viscoelastic properties (Right panel: Storage Modulus; Left Panel: Tan δ) of BIS-nBG-DG3 before and after 30 days interaction with SBF.

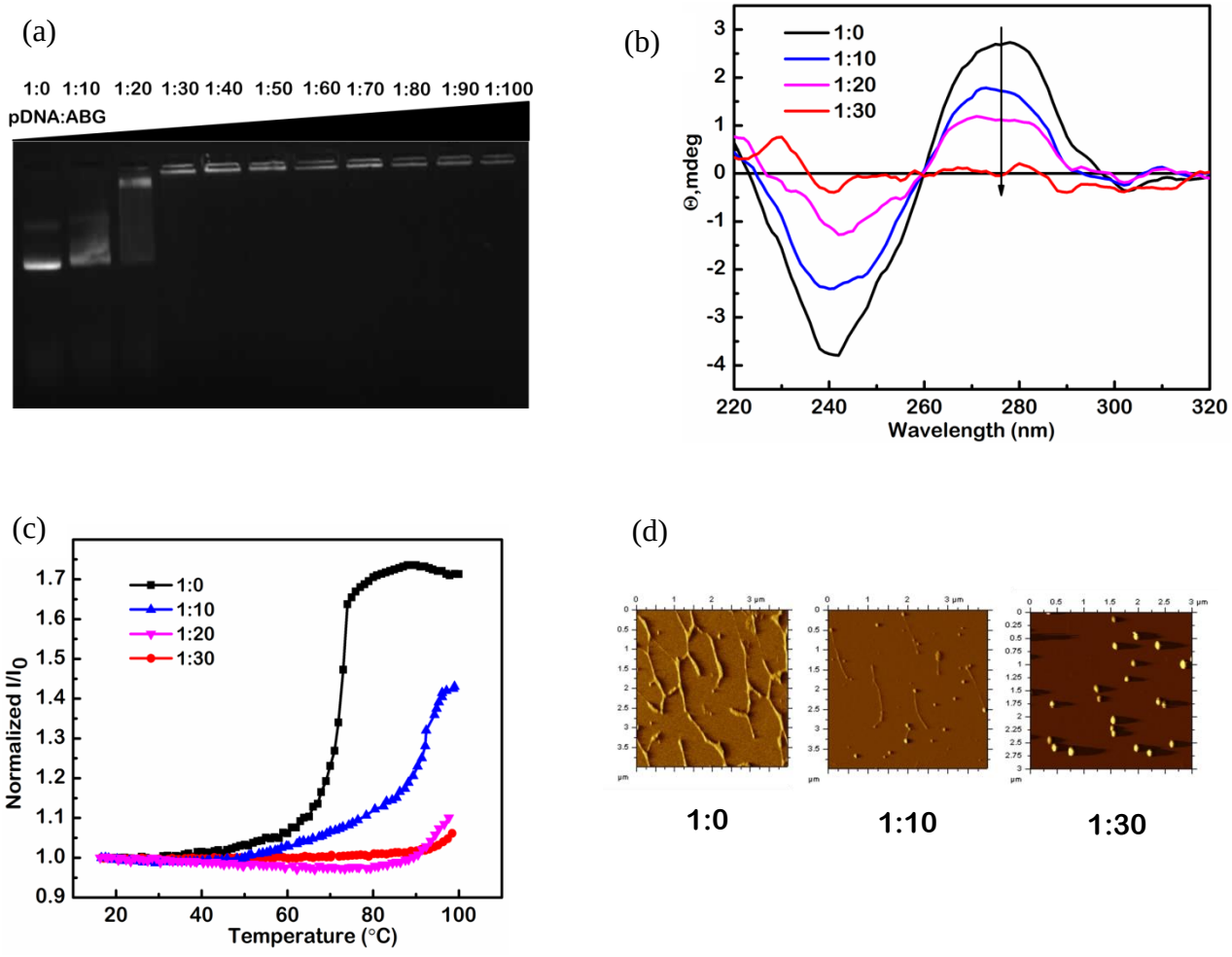

Fig. 14. *In vitro* studies result for pDNA:ABG interacted complex- (a) Gel electrophoresis assay (b) CD (c) UV-melting (d) AFM images for the pDNA:ABG at different weight ratio (µg:µg) as mentioned for the respective figures.

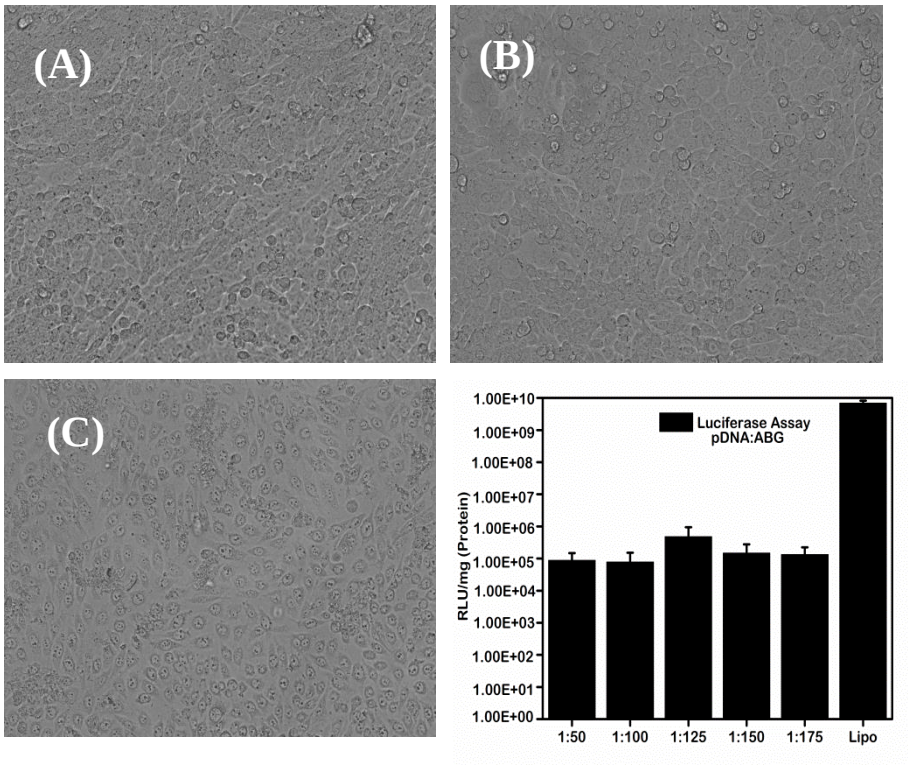

Fig. 15. Transfection efficiency studies result for pDNA:ABG complex against CHO-K1 cell line. Optical images of (a) Negative control (b) Positive control (Lipo) (c) pDNA: ABG complex of 1:125 after 24 h of interaction. Graph represents luciferase assay result of the pDNA: ABG complex at different weight ratio (µg:µg) of 1:50, 1:100, 1:125, 1:150, 1:175. Normalized against the untreated cells.

TOC